metals

MDPI

Article

An Anisotropic Damage Model for Prediction of Ductile Fracture during Cold-Forging

Atsuo Watanabe [1], Kunio Hayakawa [2,*] and Shinichiro Fujikawa [1]

[1] Nissan Motor Co., Ltd., 2 Takara, Kanagawa-ku, Yokohama 220-8623, Japan
[2] Department of Mechanical Engineering, Shizuoka University, 3-5-1 Johoku, Naka-ku, Hamamatsu 432-8561, Japan
* Correspondence: hayakawa.kunio@shizuoka.ac.jp; Tel.: +81-53-478-1607

Abstract: Researchers have formulated equations of ductile fracture to simulate and predict defects in cold-forged parts, e.g., the Cockcroft–Latham criterion. However, these equations are not applicable to certain cases of fracture in forged products. This study formulates a new equation for predicting ductile fractures with better prediction accuracy than the convention by which the cost for trial-and-error design can be reduced. The equation is expressed as a second-rank symmetric tensor, which is the inner product of the stress and strain-increment tensors. The theoretical efficacy of the equation in predicting ductile fractures is verified via a uniaxial tensile test. The practicability of the equation is confirmed by applying it to the simulations of two real cold-forged components: a cold-forged hollow shaft and a flanged shaft. For the hollow shaft, the equation predicts the position where the ductile fracture would initiate, which—to the best of the authors' knowledge—is unique to this study. For the flanged shaft, the equation predicts the occurrence of diagonal cracks due to different lubrication conditions.

Keywords: ductile fracture prediction; cold-forging; finite element analysis; anisotropic damage

Citation: Watanabe, A.; Hayakawa, K.; Fujikawa, S. An Anisotropic Damage Model for Prediction of Ductile Fracture during Cold-Forging. *Metals* **2022**, *12*, 1823. https://doi.org/10.3390/met12111823

Academic Editor: António Bastos Pereira

Received: 2 September 2022
Accepted: 25 October 2022
Published: 27 October 2022

1. Introduction

Cold-forging produces metal components without requiring machining or drilling and heating of the initial slug or inter-stages. Thus, it reduces the weight and cost of forging parts. However, this process has a limit on the amount of deformation due to ductile fracture. Ductile fracture is a defect that appears as a crack in the surface or inside the forged part and affects the strength of the material. The accurate prediction of ductile fracture by finite element analysis (FEA) is required at the forging-die-design stage while reducing trial-and-error predictions at the prototype stage.

Materials undergo ductile fracture when their atoms are separated by stress. Observations of metallic crystal particles during this separation process reveal a sequence of phenomena including cleavage, growth, and coalescence of microscopic voids, slip-surface separation, and void growth due to grain-boundary diffusion. Segregation of atoms inside the material, intermetallic compounds, impurities, initial microcracks, grain boundaries, etc. followed by the generation, growth, and coalescence of microscopic voids cause singular stress fields in metals. This process ultimately leads to fracture. Benzerga et al. [1] observed void coalescence and growth in a tensile test and investigated the anisotropy of deformation and crack growth with respect to the hot-rolling direction.

It is difficult to observe the initiation and growth of each void and express them as a comprehensive dynamic model of continuum mechanics. Previous studies on ductile fracture have proposed macroscopic damage models based on various hypotheses and proved their validity and availability through experimentation. Besson [2] reviewed the outline of ductile fracture and its prediction model studied in 2010. Tekkaya et al. [3] also reviewed the latest studies and reviewed a model for predicting damage levels.

These approaches can be categorized into two types of ductile fracture prediction models: the non-coupled model, in which the damage evolution and material deformation are not coupled during the deformation analysis, and the coupled model. The non-coupled model, which is focused on in this study, is widely used along with the FEA of cold-forging processes for the prediction of forming the limit of products. Cockcroft and Latham [4] proposed the plastic deformation energy until ductile fracture as an indicator of damage, along with a prediction equation that integrated the product of maximum principal stress and equivalent strain increment into the forming process. This equation is frequently employed for its simplicity since the model has no material constant except for the threshold value. Stebunov et al. [5] improved the equation by including the third invariant of the deviator stress and applied it for the prediction of ductile fracture of extruded parts in cold-forging. Oyane et al. [6] proposed a ductile damage model assuming volumetric strain and the exertion of principal stress on a porous body with numerous voids and volumetric strain. McClintock [7,8] proposed a ductile damage model in which a void develops in the direction of the principal stress of an infinite solid with ellipsoidal cylindrical voids. Rice and Tracey [9] expressed the growth of spherical voids in an infinite solid as an equation and proposed a ductile damage model with stress triaxiality. Gonzalez et al. [10] applied several conventional non-coupled models to the ductile fracture of central bursting in the wire drawing process and proposed a new prediction model. Ran et al. [11] applied conventional non-coupled models to the ductile fracture of extruded flanged parts and investigated the characteristics of each model using the values obtained from models as a fracture criterion.

These non-coupled ductile fracture models were assumed to be isotropic in the evolution of ductile damage. However, the generation and growth of microscopic voids and cracks in the material generally depend on the direction of the stress or strain, and the damage evolution is anisotropic in nature. The loading path in the actual forging process is generally non-proportional, and the damage evolution depends on the loading direction. When a non-proportional load is applied to the void, it cannot maintain its spherical and elliptical shapes, and the damaged state is considered directional. Therefore, it is more rational to use a damage model that considers the anisotropy of damage for general plastic deformation.

The ductile fracture criterion and threshold have also been studied for many years. Bao et al. [12] conducted a tensile test, torsion test, and compression test, measured the wide range of negative to positive stress triaxiality, and identified the ductile fracture threshold as an equivalent strain value. Bai et al. [13,14] organized the equivalent strain as the ductile fracture threshold in a three-dimensional map, and they proposed that the threshold depends not only on the stress triaxiality but also on the Lode angle. In past studies, the validity was evaluated in the target test, but the scope of utilization is unclear. It is considered that there is a relation with the averaged value such as stress triaxiality, but the cut-off relationship is physically unnatural. The fracture threshold is supposed to be the equivalent strain, and there is no discussion of anisotropy. Fincato et al. [15] showed that the non-proportional loading path affects the ductile fracture threshold. It has not been clarified that the case of changing from compression to tension or which model is universally applicable. The anisotropy of damage progression is also not taken into account.

In this study, a non-coupled anisotropic damage model is proposed to predict ductile fractures in cold-forging processes. In the conventional isotropic models, stress and strain increment components in different directions may be multiplied in case of complex material flow with non-proportional load paths, which may lead to inaccurate prediction. Rationally, the stress in the same direction should be multiplied by the strain increment. Therefore, the anisotropic formulation in which the stress in the same direction should be multiplied by the strain increment is proposed. The proposed model was based on the normalized Cockcroft–Latham isotropic ductile-damage model (the conventional model).

The applicability of the proposed model was verified using uniaxial tensile tests of smooth and notched specimens of intact spheroidizing annealed steel. Then, the proposed model was applied to the cold-forging process of hollow shaft parts for examining the validity of the proposed anisotropic damage model in practical engineering issue.

2. Ductile-Fracture Prediction Model with Anisotropic Damage

2.1. Anisotropic Damage Model

General ductile fracture models are defined as the integral of a stress function over the strain path. Among them, the models of isotropic ductile-fracture prediction by Cockcroft and Latham as well as Oyane, which are shown in Equations (1) and (2), have been widely used in finite element analysis of cold-forging for damage evaluation.

$$D_{CL} \equiv \int \left(\frac{\sigma_{max}}{\overline{\sigma}}\right) \overline{d\varepsilon} \tag{1}$$

$$D_{Oyane} \equiv \int \left(1 + \frac{1}{a}\frac{\sigma_m}{\overline{\sigma}}\right) \overline{d\varepsilon} \tag{2}$$

where σ_{max} is the maximum principal stress, $\overline{\sigma}$ is the equivalent stress, σ_m is the average normal stress, a is a material constant, and $\overline{d\varepsilon}$ is the equivalent strain increment.

The damage growth is considered anisotropic in nature. Here, an anisotropic ductile-fracture theory is proposed and applied to the numerical analysis.

The product of the stress and plastic strain-increment tensors yields the specific strain energy increment dW, which is given as,

$$dW = \sigma_{ij}\, d\varepsilon_{ij} = \delta_{ij}\, (\sigma_{ik}\, d\varepsilon_{kj}) \tag{3}$$

where σ_{ij} is a stress tensor, $d\varepsilon_{ij}$ is a strain-increment tensor, and δ_{ij} is Kronecker's delta.

It can be interpreted from the tensor operation that $\overline{D}_{ij}$ is tensors having a physical meaning of specific strain energy. The tensor contraction of $\overline{D}_{ij}$ can be regarded as dW as shown in Equation (3).

Based on Equation (3), the anisotropic ductile damage model, Equation (4) is proposed, which is a second-order tensor ductile damage model as a possible modification of general ductile fracture evaluation models.

$$\overline{D}_{ij} = \int \frac{\sigma_{ik}}{\overline{\sigma}} d\varepsilon_{kj} \tag{4}$$

The effect of the directions of stress and strain can be considered in ductile damage evolution analysis by Equation (4).

As Equation (4) is an asymmetric tensor, the principal damage values may be complex numbers, which makes physical interpretation difficult. Therefore, an anisotropic ductile fracture evaluation equation of Equation (5) is proposed in this paper, which is a symmetrized form of Equation (4) using the method that Murakami [16] employed to the effective stress in continuum damage mechanics.

$$\overline{\overline{D}}_{ij} = \frac{1}{2}\int \left(\frac{\sigma_{ik}}{\overline{\sigma}} d\varepsilon_{kj} + \frac{\sigma_{jl}}{\overline{\sigma}} d\varepsilon_{li}\right) \tag{5}$$

It is convenient to use the principal damage value of Equation (5) when discussing anisotropic ductile damage. Under the cylindrical coordinate system O-$r\theta z$, the principal damage values $\overline{\overline{D}}_{\mathrm{I}}$, $\overline{\overline{D}}_{\mathrm{II}}$ and $\overline{\overline{D}}_{\mathrm{III}}$ are given by Equation (6) using the components of $\overline{\overline{D}}_{ij}$; $\overline{\overline{D}}_r$, $\overline{\overline{D}}_\theta$, $\overline{\overline{D}}_z$ and $\overline{\overline{D}}_{rz}$.

$$\left.\begin{matrix}\overline{\overline{D}}_I \\ \overline{\overline{D}}_{II}\end{matrix}\right\} = \frac{1}{2}\left(\overline{\overline{D}}_r + \overline{\overline{D}}_z\right) \pm \sqrt{\left(\frac{\overline{\overline{D}}_r - \overline{\overline{D}}_z}{2}\right)^2 + \overline{\overline{D}}_{rz}^2},\ \overline{\overline{D}}_{III} = \overline{\overline{D}}_\theta \tag{6}$$

Then the ductile fracture criterion using Equation (5) is based on the presumption that the local ductile fracture will occur when the maximum principal value $\overline{\overline{D}}_{max}$ of $\overline{\overline{D}}_{ij}$ attains a certain threshold value D_c. This is based on the presumption that microscopic cracks often initiate in the direction perpendicular to the maximum principal stress direction. Therefore, the proposed ductile fracture criterion can be expressed as follows:

$$\overline{\overline{D}}_{max} = D_c \tag{7}$$

In the proposed equation, only the anisotropy of the damage progression is considered. Practically, there may be anisotropy in the fracture threshold D_c due to the influence of the residual strain in the previous process or the distribution of the segregation of steel materials and so on. If the fracture threshold of the material is anisotropic, D_c may be different depending on the direction. In this study, spheroidizing annealing is conducted before the experiment to assume that the fracture threshold D_c is isotropic.

2.2. Damage Equation Considering Compressive Stress

In forging processes, parts are subjected to both tensile stress and compressive stress during the processes. The influence of compressive stress on damage evolution cannot be ignored depending on the type of material. In this paper, it is assumed that damage develops with compressive stress as well as tensile stress. The stress components inside the material are different in direction and magnitude depending on its coordinate system. Here, the ductile damage is expressed under the principal direction. We adopt a modified stress tensor $\widetilde{\sigma}_{ij}$ considering the reduced compressive stress effect to damage evolution as given in Equation (8) in the principal stress coordinate system.

$$[\widetilde{\sigma}] = \begin{bmatrix} \langle\sigma_1\rangle & 0 & 0 \\ 0 & \langle\sigma_2\rangle & 0 \\ 0 & 0 & \langle\sigma_3\rangle \end{bmatrix} - \alpha \begin{bmatrix} \langle-\sigma_1\rangle & 0 & 0 \\ 0 & \langle-\sigma_2\rangle & 0 \\ 0 & 0 & \langle-\sigma_3\rangle \end{bmatrix} \tag{8}$$

where, α is the material constant expressing the reduced effect of compressive stress to damage evolution, and the bracket < > is Macaulay brackets. α = 0 and 1 mean full- and no-reduction of the effect, respectively. The flow of calculation of this equation is shown in Figure 1. The stress and strain increment tensors in the principal direction are calculated, and the stress in consideration of the compressive direction is calculated by Equation (8). The increment of ductile damage is calculated in the principal direction. However, the principal direction changes during the forging process. Therefore, the increment of damage in the principal direction is converted to that in the global coordinate system, and the damage values are accumulated in the global coordinate system.

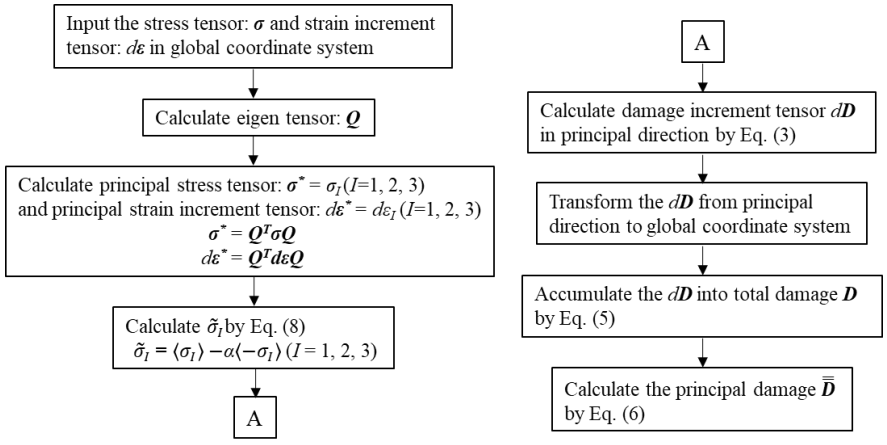

Figure 1. Calculation flow chart of damage equation considering compressive stress.

3. Verification of the Anisotropic Damage Model by Uniaxial Tensile Test

3.1. Experimental Condition

The round bar specimen was subjected to the uniaxial tensile test to measure the flow stress and the fracture threshold value in Equation (7). Figure 2 shows the dimensions of the specimen. For a smooth cylindrical specimen, however, the displacement undergoes a significant change of approximately 0.5 mm at fracture when measured in three successive iterations. Therefore, in this study, the notched cylindrical tensile specimen was used to evaluate the threshold calculated with the round bar specimen (Figure 3). In this case, the dispersion of displacement at fracture was approximately 0.02 mm after three iterations. For the notched cylindrical tensile specimen, two types of radii (*c* in Figure 3) were prepared. This is because the damage values at fracture are compared to elucidate the difference in the stress triaxiality of the fracture criterion.

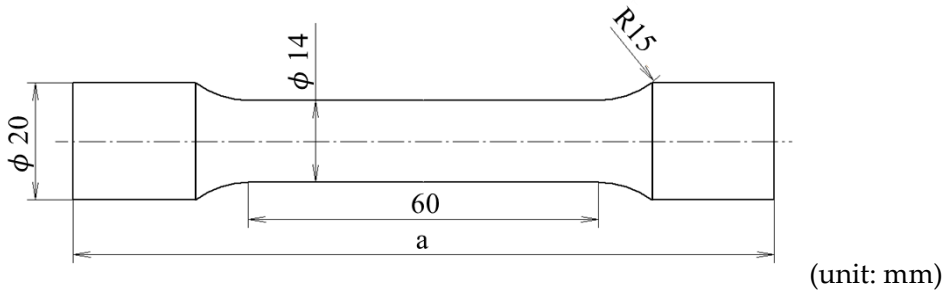

Figure 2. Smooth round bar specimen for uniaxial tensile test (a: 80, 90, or 120).

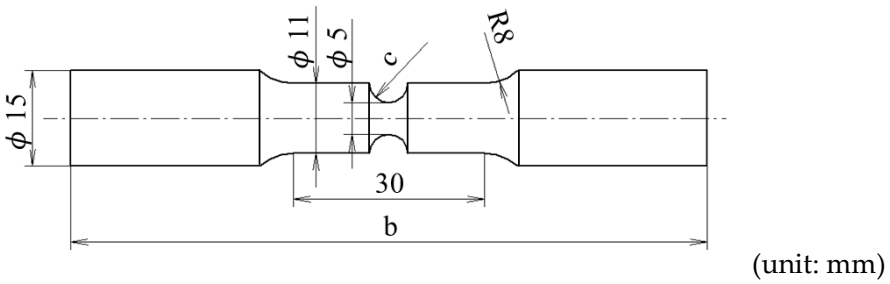

Figure 3. Notched round bar specimen for tensile test (b: 80, 90, or 100, c: R1 or R3).

Chromium steel SCr420H (in JIS) was applied as a material with high ductility. Table 1 lists the chemical composition of the material. Before the tensile tests, specimens were spheroidized under 730 °C for 10 h and furnace-cooled (Specimen A) or 690 °C for 10 h and furnace-cooled (Specimen B). The inner hardness of Specimens A and B before the tensile test were 78.9 and 80.2 HRB, respectively. Specimen A had a smaller hardness value because it was spheroidized at a higher temperature than Specimen B.

Table 1. Chemical composition of SCr420H.

Material	C	Si	Mn	P	S	Cr	Fe
SCr420H	0.20	0.25	0.73	0.03	0.03	1.05	Bal.

It is noted that the hardness value was obtained by averaging the results of seven specimens. A maximum difference of 1.2 HRB was confirmed in each measurement result. There was no clear significant difference in the hardness measurement result. Figure 4 shows microstructure observation between specimens A and B. It was confirmed that the higher temperature, the more spheroidization of cementite increases.

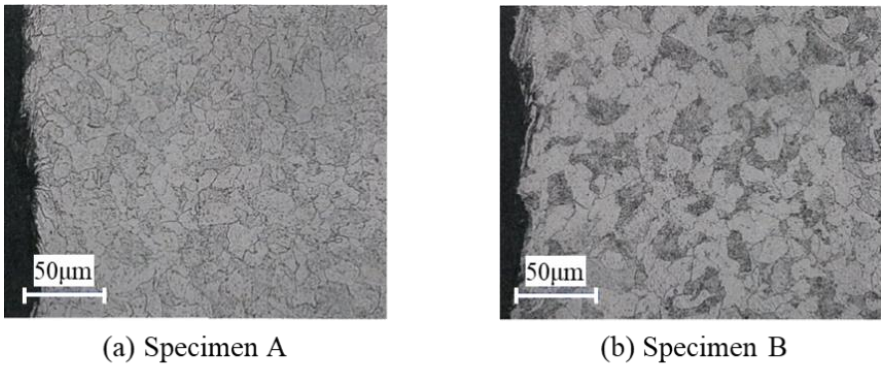

Figure 4. Microstructure observation.

A series of tensile tests was conducted to verify the influence of prior compression to uniaxial tensile test on the fracture limit value, in order to clarify the effect of the introduction of Equation (8). Figure 5 shows the preparation procedure of the uniaxial tensile specimen subjected to prior compression. Specimen A was used for the experiments. The material with 45.0 mm in diameter and 120.0 mm in height was compressed to a height of 90.0 mm (25% compression) and 80.0 mm (33% compression) using a 4.9 MN hydraulic press. Then, the uniaxial tensile specimens were prepared with lengths *a* and *b* in Figures 2 and 3 according to the compression ratio, from the compressed material as shown in Figures 2 and 3. The specimens prepared are listed in Table 2.

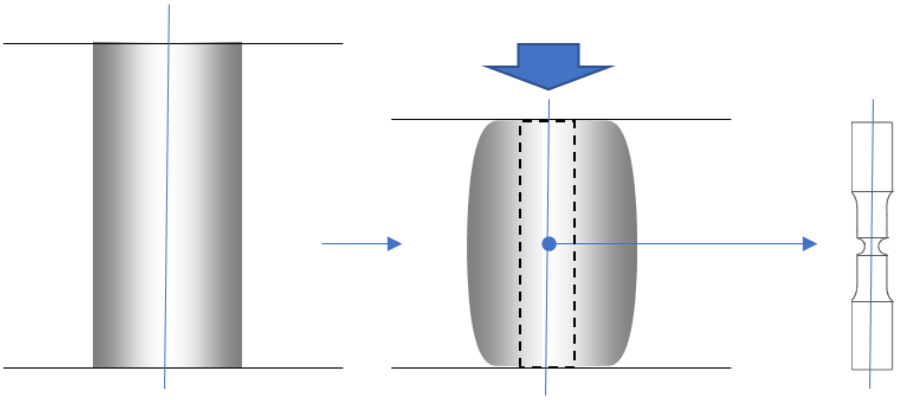

Figure 5. Schematics of tensile test after the compressive test.

Table 2. List of tensile tests.

No.	Spheroidizing Annealing	Specimen Type	Reduction in Prior Compression	Specimen Length a/mm	Specimen Length b/mm	Radius of Notch c/mm
1	Specimen A (730 °C, 10 h, furnace cooling)	Smooth	-	120	-	-
2		Notched	25%	90	-	-
3			33%	80	-	-
4			-	-	100	R3
5			25%	-	90	R3
6			33%	-	80	R3
7			-	-	100	R1
8	Specimen B (690 °C, 10 h, furnace cooling)	Smooth	-	120	-	-
9		Notched	-	-	100	R3

3.2. Experimental Result

The stress-strain curves were obtained from the tensile test using a smooth round bar specimen as shown in Figure 2. Material constants F, n, and ε_0 of Swift's law $\sigma = F(\varepsilon + \varepsilon_0)^n$ were determined by the trial-and-error approximation of the equation to the experimental results. Table 3 shows the material constants obtained according to Swift's law. Since the temperature of the spheroidizing annealing is higher, material constant F of Specimen A is smaller, and the flow stress is lower than that of Specimen B. Figure 6 shows the stress-strain curves of Specimen A. For the uniaxial tensile test using the specimen without prior compression, fracture occurs at the equivalent strain of 0.13. The stress-strain curve was extrapolated up to a large strain region using the results of the tensile test after compressing the height to 25% and 33%, as Hering et al. [17] applied to the pre-strained and damaged steel.

Table 3. Material constants of Swift's law of SCr420H.

Spheroidizing Annealing	Plasticity Coefficient F/MPa	Work Hardening Exponent n	Material Constant ε_0
Specimen A	730	0.14	0.001
Specimen B	889	0.17	0.003
			$\sigma = F(\varepsilon + \varepsilon_0)^n$

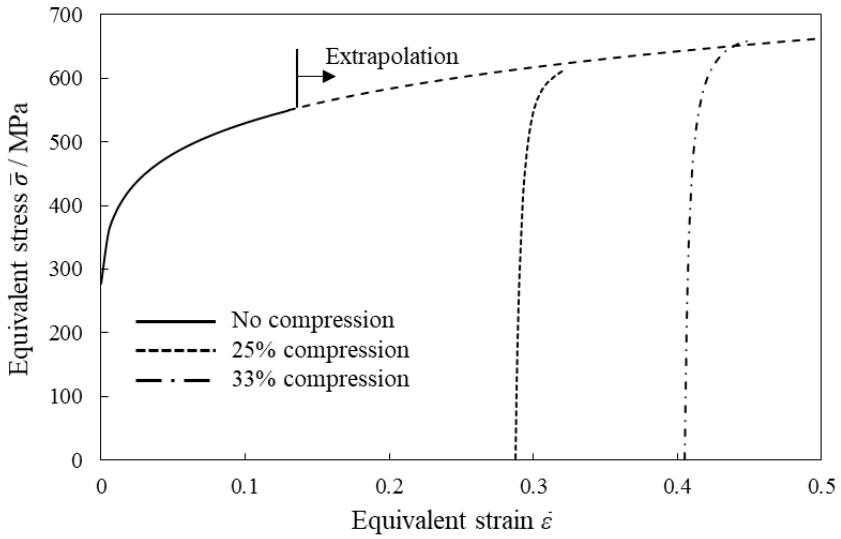

Figure 6. Stress-strain curve of Specimen A.

Using the stress-strain curves in Table 3 and Figure 6, finite element analysis of the tensile test of the notched round bar specimen was conducted. The axisymmetric elasto-plastic FEA was performed on DEFORM-2D (SFTC). Equations (5) through (7) were implemented in the software by the user subroutine functionality to calculate the principal value of the damage value at fracture. Figure 7 shows the simulation model. The same forced displacement as the actual measurement was applied as the boundary condition according to the position of the gauge of the testing machine with a length of 12.5 mm. The total number of elements was about 5000 and the size of the elements at the fracture position was 0.08 mm. The calculation step was 1.0 s/step, and the displacement speed was the same as the actual measurement. The calculation was stopped when the displacement reached that at fracture in the experiment. The load-displacement curves by the simulation and the experiment are shown in Figures 8 and 9. Figure 8 shows the result of the specimens without pre-compression. Figure 9 shows the results of pre-compressed specimens. Good accordance was observed between simulated and experimental results in each figure.

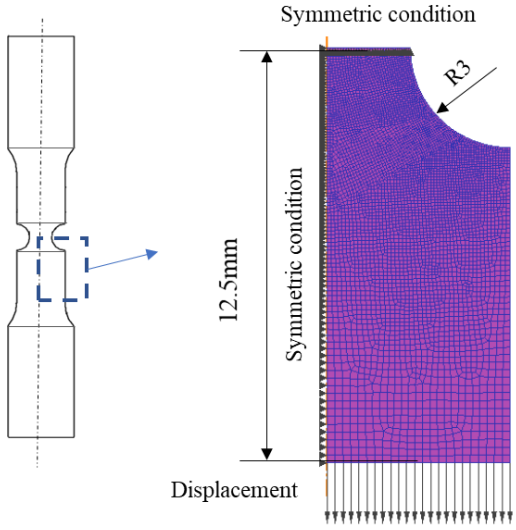

Figure 7. Simulation model of tensile test (Notched round bar specimen No. 4 in Table 2).

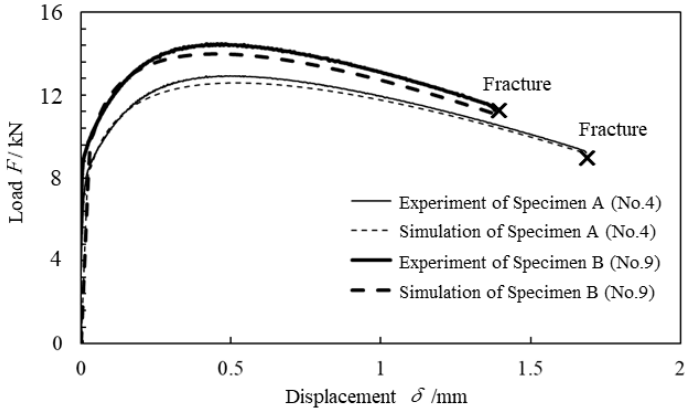

Figure 8. Load–displacement relationship in the uniaxial tensile test of notched round bar specimen without prior compression.

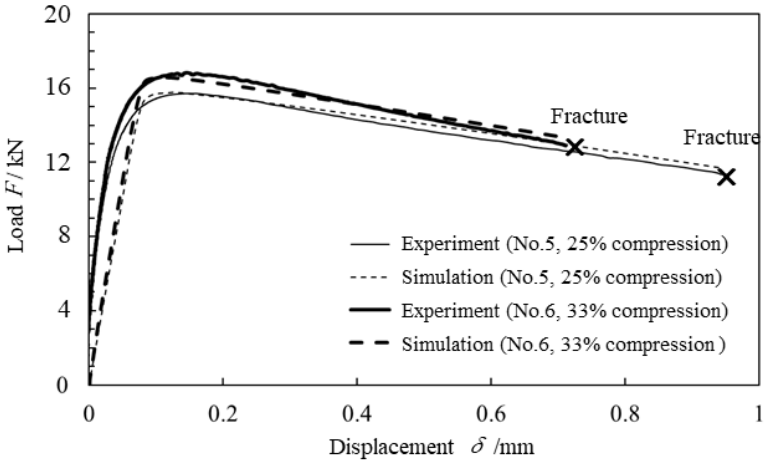

Figure 9. Load–displacement relationship in the uniaxial tensile test of notched round bar specimen with prior compression (Specimen A).

Figure 10 shows the distribution of the maximum principal damage value $\bar{\bar{D}}_{max}$ of $\bar{\bar{D}}_{ij}$ as calculated by Equation (6). This result was No.4 in Table 2. Additionally, Figure 11 shows $\bar{\bar{D}}_{max}$ along the radial coordinate r of the fractured surface. The component $\bar{\bar{D}}_z$ dominates

the test because $\bar{\bar{D}}_z$ and $\bar{\bar{D}}_{max}$ have nearly identical values. As shown in Figure 11, Specimen A has a larger $\bar{\bar{D}}_{max}$ than Specimen B at fracture. Therefore, the former has a larger ductile-fracture threshold. The largest predicted value occurs at the center of the specimen (Figure 10), implying that the fracture is initiated at the center if it has a uniform threshold. However, the initiation of fracture could not be clarified by this experiment.

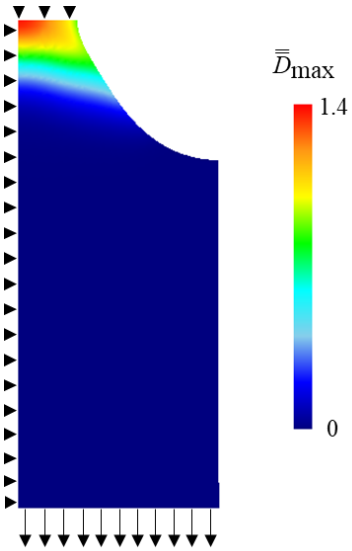

Figure 10. Distribution of the maximum principal damage value at fracture in the uniaxial tensile test of notched round bar specimen (No.4 in Table 2).

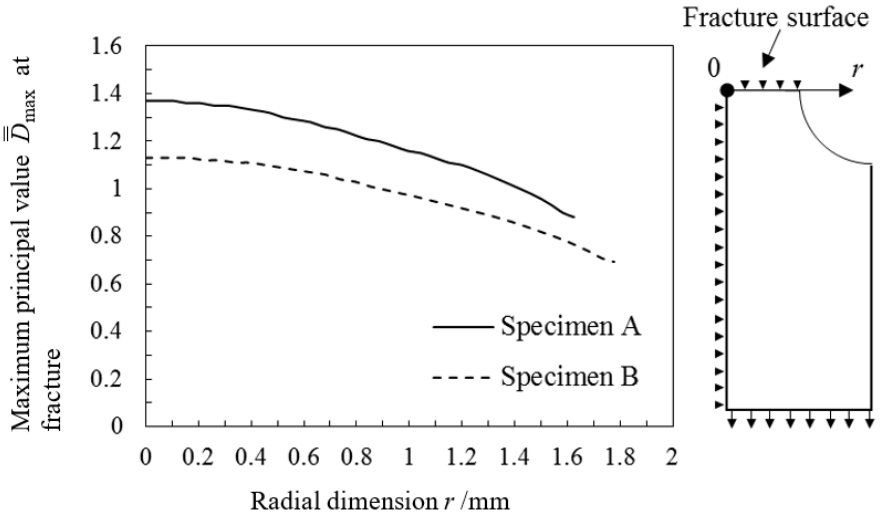

Figure 11. Change in the maximum principal damage values to the radial dimension at fracture surface of notched round specimens (No. 4 and No. 9 in Table 2).

Figure 12 shows the simulation results on the change in $\bar{\bar{D}}_{max}$ on the uniaxial loading of the notched round bar of Specimen A subjected to prior compression. The subsequent uniaxial loading simulations were performed by inheriting the information on stress, strain, and damage by the prior compression simulations, as the same procedure as experiments shown in Figure 5. In the case of α = 0.0 in Equation (8), no effect of compression to damage evolution, $\bar{\bar{D}}_{max}$ at fracture is much lower than that of no prior compression. In the case of α = 1.0, the full effect of compression to damage evolution, the damage value at fracture is slightly lower than that of no prior compression. From the results above, it was observed that damage evolution is in progress even in the process where compressive stress is dominating.

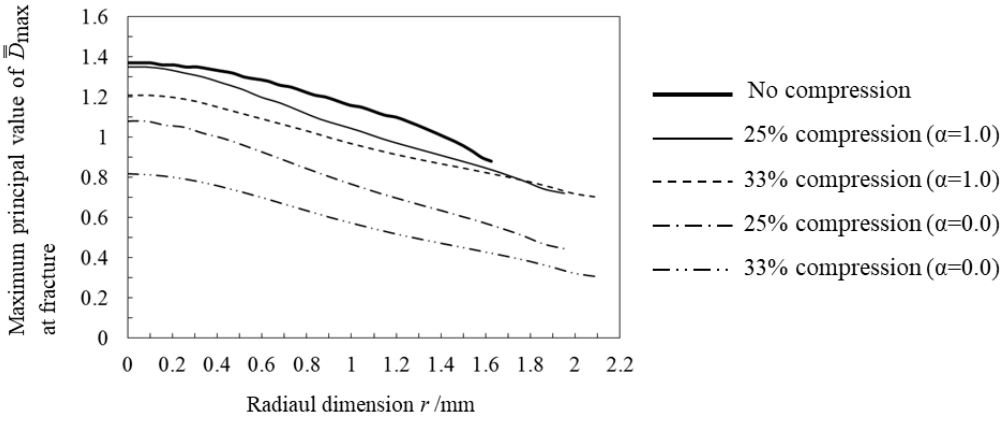

Figure 12. Change in maximum principal damage using compressed specimen (Specimen A).

It is considered that the reason for the decrease in $\bar{\bar{D}}_{max}$ is the effect of σ_{tri}. The decrease in $\bar{\bar{D}}_{max}$ when considering the damage value of compression at α = 1.0 results from the increase of $\sigma_{tri} = \sigma_m / \sigma$ due to strain hardening by prior compression. The change in $\bar{\bar{D}}_{max}$ to σ_{tri} is shown in Figure 13, where $\bar{\bar{D}}_{max}$ is the value at the center of the specimen. It is observed that $\bar{\bar{D}}_{max}$ is correlated with σ_{tri}.

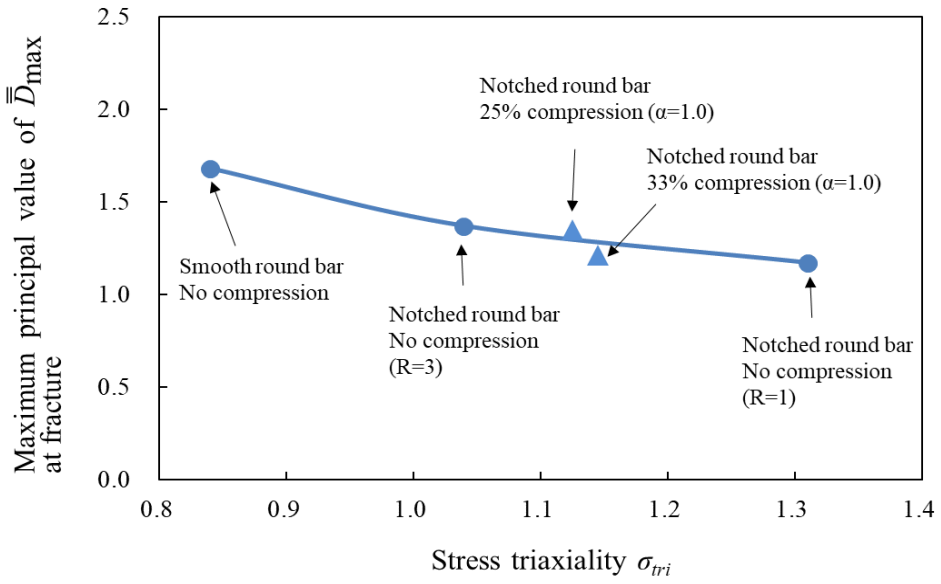

Figure 13. Maximum principal damage change against stress triaxiality (Specimen A).

4. Application of Anisotropic Damage Model for Prediction of Ductile Fracture in Hollow Shaft Parts

4.1. Forging Process of Hollow Shaft Parts

Figure 14 shows the cold-forging process of hollow shaft parts, which consists of pre-forming, backward extrusion, and multiple forward extrusions. The weight of the part may be approximately 40% less than the solid shaft. The part was made of steel S48C (in JIS). Before pre-forming and multiple forward extrusions, the part was spheroidized and treated with a phosphate coating for lubrication.

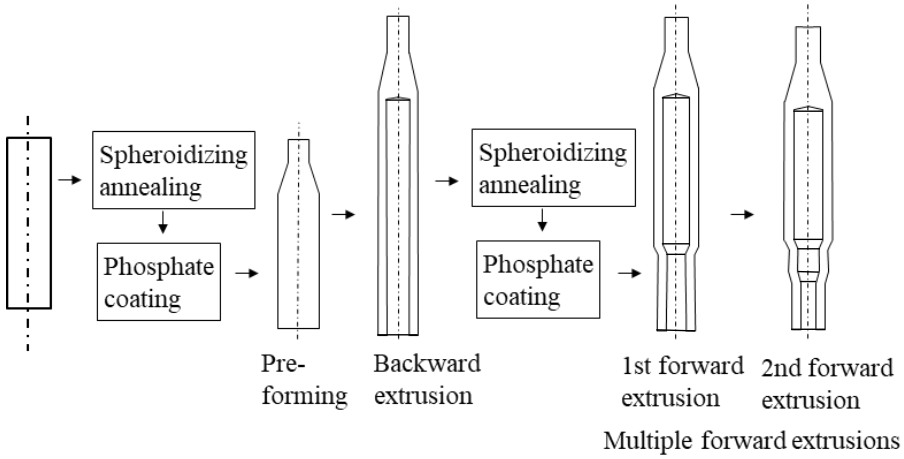

Figure 14. Sequence of cold-forging operations of hollow shaft parts.

The conditions of spheroidizing annealing were a holding temperature of 750 °C and a holding time of 13 h. A hydraulic press of 16 MN was used for manufacturing the part at an average press speed of 45 mm/s. The length, and outer and inner diameters of the workpiece after backward extrusion were 287.5, 46.2, and 31.0 mm, respectively. The strokes of the first and second forward extrusions were 80.0 and 66.5 mm, respectively. The outer diameters of the part after the first and second forward extrusions were 38.6 and 31.8 mm, respectively.

4.2. Application of Isotropic Ductile Damage Model

Ductile fracture (crack) was observed at the edges of the hollow shaft parts after the first extrusion process as shown in Figure 15. The fracture further developed at the second forward extrusion. The defect was able to be suppressed by changing the spheroidizing annealing temperature to 765 °C from the previous one of 750 °C.

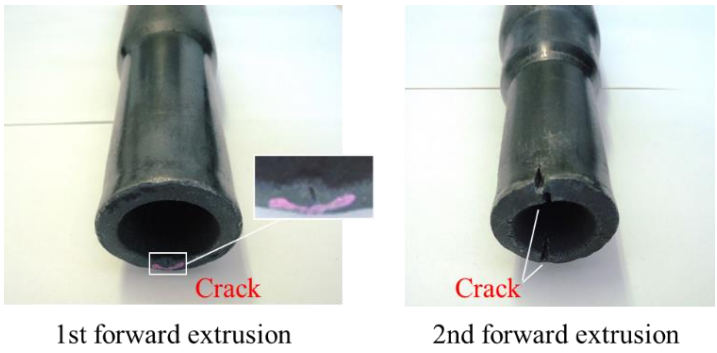

Figure 15. Ductile fracture of hollow shaft parts.

Numerical simulation was applied to the process to confirm whether the conventional ductile damage models can predict the ductile fracture in this process. The axisymmetric elastic-plastic FEA was performed by DEFORM-2D (SFTC). The flow stress data for the analysis were obtained from a compression test of a cylindrical specimen (diameter: 10 mm, height: 15 mm). Figure 16 shows the obtained flow stress curve. The analysis used a shear friction coefficient m of 0.03 and quadrilateral elements with an initial element size of 1.0 mm. The calculation step was 0.05 mm/step, the die model was a rigid body, and the die speed was set to 45 mm/s according to the actual measurement. Figure 17 shows the dimension of the first extrusion process and the FEA model.

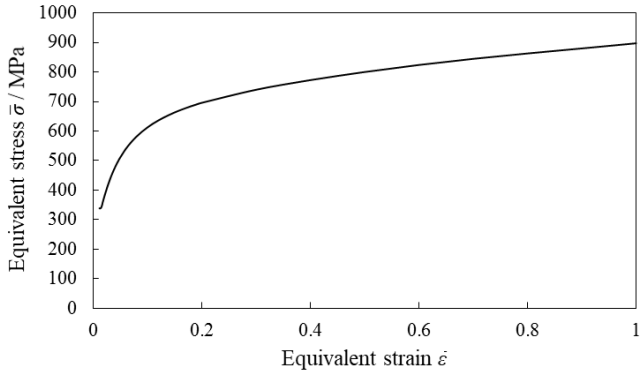

Figure 16. Flow curve of material of cold-forged hollow shaft S48C.

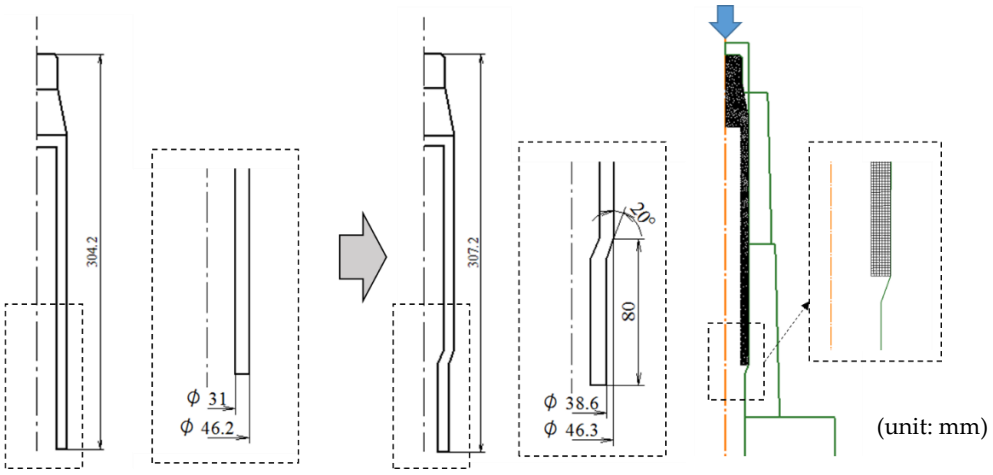

Figure 17. The dimension of first forward extrusion and FEA model.

Figure 18 shows the comparison of the dimensions A, B, ϕC ~ ϕE between the simulation results and the actual forged parts in the first forward extrusion process. The absolute dimensional error was within 1 mm, which is equivalent to the maximum relative error of approximately 0.3%. Thermal effect was not considered here and hereafter, since the difference in dimensional values after deformation was about 0.2% in the case of coupled thermal and deformation analysis, from which it was judged that the effect of temperature change on damage development was negligible.

Figure 19 shows the simulation results of isotropic ductile-fracture predictions by conventional ductile-damage models D_{CL} and D_{Oyane} by Equations (1) and (2) at the end of the first forward extrusion process. Though Oyane et al. [6] determined the material constant $a = 0.28$ from copper's experiment, this value is different for the material. Therefore, the material constant a for D_{Oyane} was changed to 0.02, 0.2 and 2.0 in this paper. From the figure, it is observed that the regions of maximum D_{CL} and D_{Oyane} do not coincide with the region where actual ductile fracture occurred.

Here the disagreement in the case of D_{CL} will be discussed. The detailed investigation of change in the D_{CL} at point A in Figure 19a revealed that the rapid increases of D_{CL} from the stroke S_1 of approximately 15 mm were observed. The change in strain components ε_r, ε_θ, ε_z and equivalent strain $\bar{\varepsilon}$ at point A on the cylindrical coordinate system O-$r\theta z$ (r, θ, and z indicate the radial, circumferential, and axial directions) are depicted in Figure 20, which is helpful for understanding the behavior of D_{CL}, where the absolute value $|\varepsilon_\theta|$ was displayed since ε_θ takes a negative value during the process. Since the region near point A was subjected to a monotonic compression in the θ direction as a result of the reduction of the inner diameter, $|\varepsilon_\theta|$ monotonically increased during the process. The change in $\bar{\varepsilon}$ is similar to $|\varepsilon_\theta|$, which follows that the strain component $|\varepsilon_\theta|$ is more predominant than others.

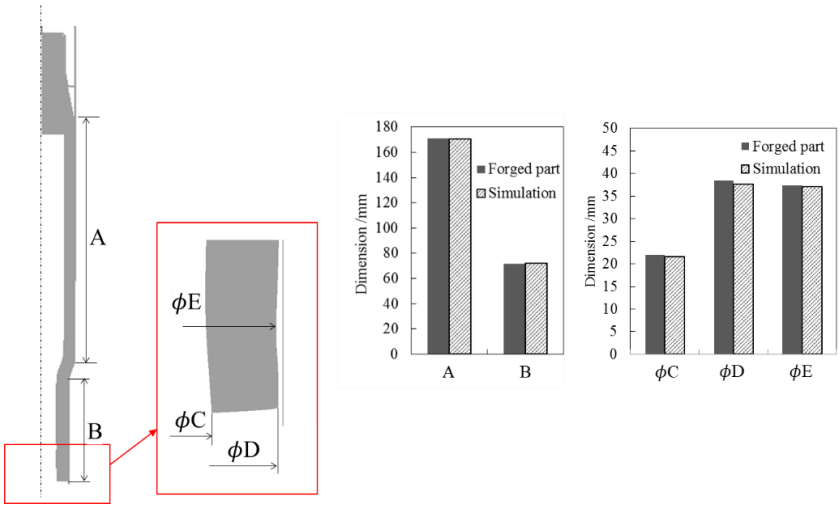

Figure 18. Comparison of the dimensions between the simulation results and the actual forged parts in the first forward extrusion process.

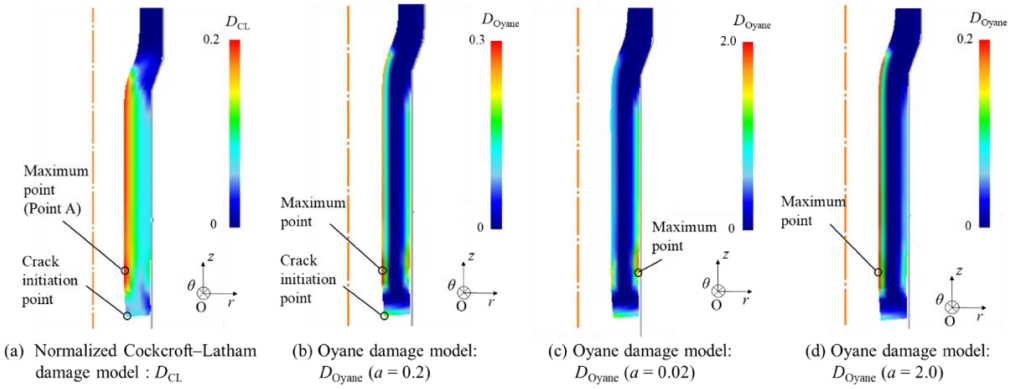

Figure 19. Isotropic ductile-fracture prediction by conventional isotropic ductile-damage model in first forward extrusion.

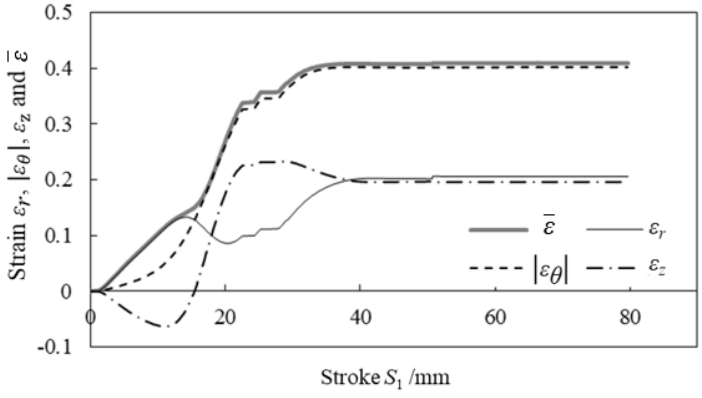

Figure 20. Strain variation in first forward extrusion.

On the other hand, Figure 21 shows the change in stress components σ_r, σ_θ, σ_z and maximum principal stress σ_{max} at point A. Since σ_{max} from S_1 = 15 mm changes similar to σ_z, the σ_z is a more predominant component than the others during the process.

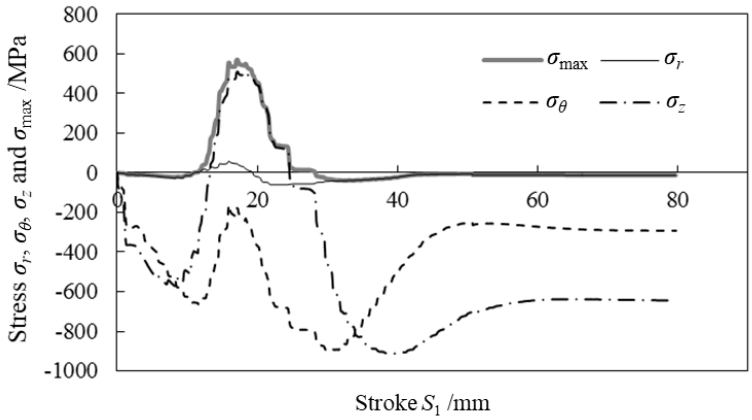

Figure 21. Stress variation in first forward extrusion.

From the above and Equation (1), it confirms that the predominant stress and strain increment components in different directions at point A were used to evaluate the ductile fracture in the case of D_{CL}. Similar consideration holds in the case of D_{Oyane}, too. Therefore, it will be not plausible to use these models in the process depicted in Figure 14.

4.3. Application of Anisotropic Damage Model

Figure 22 shows the distributions of D_{CL} and $\bar{\bar{D}}_{max}$ in Equations (1) and (5), respectively. The proposed damage model in Figure 22b enables the convergence of the crack-initiation position in the ductile fracture of the actual part and the position with the greatest damage. In the case of D_{CL} in Figure 22a as mentioned in Section 4.2, however, the maximum value did not coincide with the ductile fracture position.

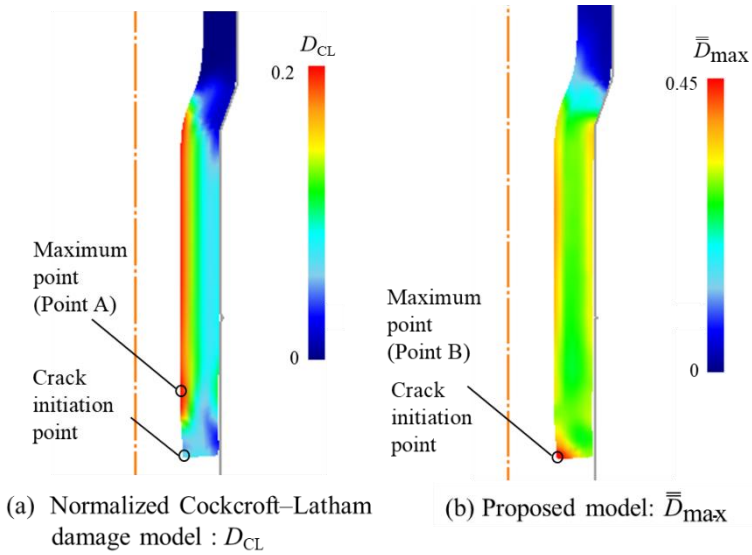

Figure 22. Distribution of ductile damage in first forward extrusion.

It was found that the damaged component $\bar{\bar{D}}_{III} = D_\theta$ in Equation (6) behaved akin to $\bar{\bar{D}}_{max}$ in this case. Therefore, the behaviors of stress and strain increment in the θ direction were examined. Figure 23 shows the change in σ_θ and $d\varepsilon_\theta$ to S_1 in the first forward extrusion. Both values increase at S_1 = 20 mm where the damage value increases. From the fact that the direction of the crack surface in Figure 23 was perpendicular to the θ direction, it follows that the proposed anisotropic ductile fracture damage model was able to predict the accumulation of damage in the θ direction.

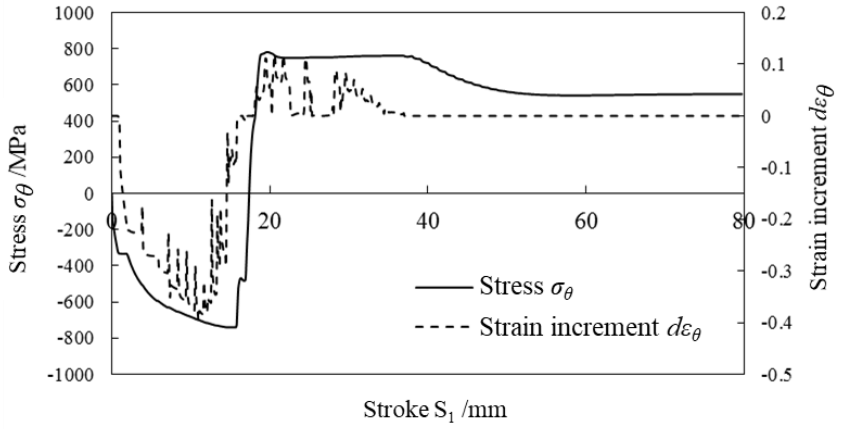

Figure 23. Change in Normal stress and strain rate along the θ direction to stroke in the first forward extrusion.

The fracture shown in Figure 15 was able to be suppressed in practice by increasing the temperature of the spheroidizing annealing to 765 °C from 750 °C due to the increase of ductility. From the above, the ductile fracture threshold D_c in Equation (7) in the second extrusion process was attempted to be determined here. The D_c is obviously larger than that in Figure 22b, $D_c > 0.45$.

The geometry shown in Figure 24 was applied to the second forward extrusion. As shown in the table in Figure 24, different $\bar{\bar{D}}_{max}$s were predicted by changing outer diameters ϕA and the cross-section reduction rates *Re* of the edge of the second forward extrusion process. In the calculations, the flow stress of the spheroidizing annealed material at a temperature of 765 °C was employed, and other analysis conditions were also the same as in Section 4.2.

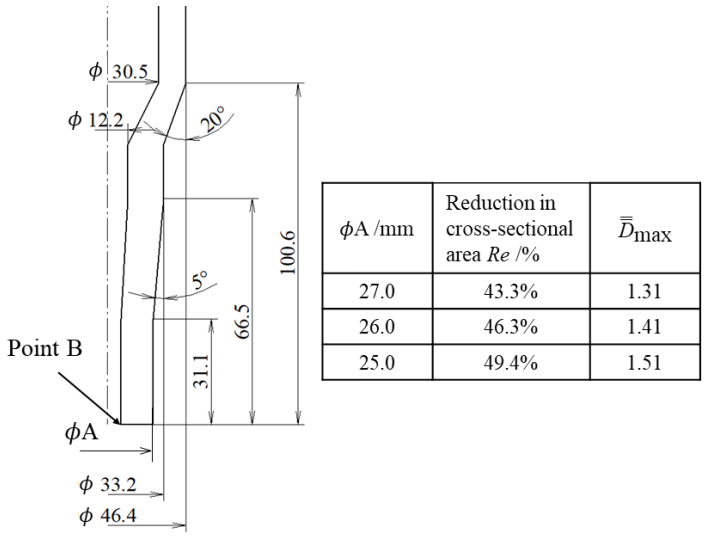

ϕA /mm	Reduction in cross-sectional area *Re* /%	$\bar{\bar{D}}_{max}$
27.0	43.3%	1.31
26.0	46.3%	1.41
25.0	49.4%	1.51

Figure 24. Reduction in cross-sectional area and calculated damage in second forward extrusion.

Figure 25 shows the change in $\bar{\bar{D}}_{max}$ at the edge of the inner diameter of the shaft where the ductile fracture occurs (Point B in Figure 24). The horizontal axis is the stroke *S* consisting of the first and second extrusion strokes. $\bar{\bar{D}}_{max}$ for each *Re* is summarized in the table in Figure 24. Subsequently, forging tests with the different *Re*s were performed. Six tests were performed for each *Re*. As a result, there was no ductile fracture in the cases of $\bar{\bar{D}}_{max}$ = 1.31 (*Re* = 43.3%) and 1.41 (*Re* = 46.3%). In the case of *Re* = 49.4% of $\bar{\bar{D}}_{max}$ = 1.51

(*Re* = 49.4%), ductile fracture occurred in one piece out of six pieces. Therefore, the ductile fracture threshold was supposed to be determined as follows:

$$\bar{\bar{D}}_{max} = D_c > 1.41 \quad (9)$$

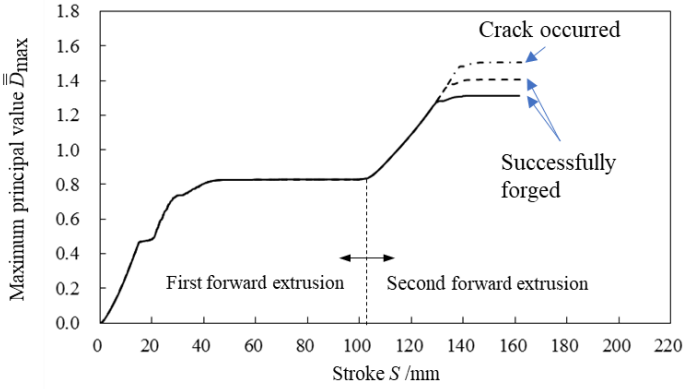

Figure 25. Change in ductile fracture value during multiple forward extrusion processes.

5. Conclusions

In the case of a complex loading history and material flow such as in cold-forging, the conventional isotropic damage model may not accurately predict the position of ductile failure. Therefore, a damage model of ductile fracture considering the anisotropy of deformation and crack growth was proposed. The findings led to the following conclusions. Although there are still only a few application examples, the proposed model is considered to be applicable to problems that cannot be properly predicted by the conventional isotropic ductile fracture models.

1. In the proposed equation of anisotropic ductile fracture, the degree of damage is expressed by the product of the stress and strain increment tensors. The threshold value of ductile fracture was verified by a tensile test. The effectiveness of the damage equation was confirmed.

2. The position of the ductile fracture coincided with the calculated damage value when the proposed equation was applied to the cold-forging of hollow shaft parts.

Author Contributions: Conceptualization, A.W., K.H. and S.F.; methodology, A.W. and K.H.; software, A.W.; validation, A.W., K.H. and S.F.; investigation, A.W.; resources, A.W.; data curation, A.W.; writing—original draft preparation, A.W.; writing—review and editing, K.H.; visualization, A.W.; supervision, K.H. All authors have read and agreed to the published version of the manuscript.

Funding: This research received no external funding.

Informed Consent Statement: Not applicable.

Conflicts of Interest: The authors declare no conflict of interest.

References

1. Benzerga, A.A.; Besson, J.; Pineau, A. Anisotropic ductile fracture Part I: Experiments. *Acta Mater.* **2004**, *52*, 4623–4638. [CrossRef]
2. Besson, J. Continuum Models of Ductile Fracture: A Review. *Int. J. Damage Mech.* **2010**, *19*, 3–52. [CrossRef]
3. Tekkaya, A.E.; Bouchard, P.-O.; Bruschi, S.; Tasan, C.C. Damage in metal forming. *CIRP Ann.—Manuf. Technol.* **2020**, *69*, 600–623. [CrossRef]
4. Cockcroft, M.G.; Latham, D.J. Ductility and workability of metals. *J. Inst. Met.* **1968**, *96*, 33–39.
5. Stebunov, S.; Vlasov, A.; Biba, N. Prediction of fracture in cold forging with modified Cockcroft-Latham criterion. *Procedia Manuf.* **2018**, *15*, 519–526. [CrossRef]
6. Oyane, M.; Sato, T.; Okimoto, K.; Shima, S. Criteria for ductile fracture and their applications. *J. Mech. Work. Technol.* **1980**, *4*, 65–81. [CrossRef]
7. McClintock, F.A.; Kaplan, S.M.; Berg, C.A. Ductile fracture by hole growth in shear bands. *Int. J. Fract. Mech.* **1966**, *2*, 614–627. [CrossRef]
8. McClintock, F.A. A criterion for ductile fracture by the growth of holes. *J. Appl. Mech.* **1968**, *35*, 363–371. [CrossRef]

9. Rice, J.R.; Tracey, D.M. On the ductile enlargement of voids in triaxial stress fields. *J. Mech. Phys. Solids* **1969**, *17*, 201–217. [CrossRef]
10. Gonzalez, A.A.; Celentano, D.J.; Cruchaga, M.A. Assessment of ductile failure models in single-pass wire drawing processes. *Int. J. Damage Mech.* **2017**, *27*, 1291–1306. [CrossRef]
11. Ran, J.Q.; Fu, M.W. Applicability of the uncoupled ductile fracture criteria in micro-scaled plastic deformation. *Int. J. Damage Mech.* **2016**, *25*, 289–314. [CrossRef]
12. Bao, Y.; Wierzbicki, T. On fracture locus in the equivalent strain and stress triaxiality space. *Int. J. Mech. Sci.* **2004**, *46*, 81–98. [CrossRef]
13. Bai, Y.; Wierzbicki, T. Application of extended Mohr–Coulomb criterion to ductile fracture. *Int. J. Fract.* **2010**, *161*, 1. [CrossRef]
14. Bai, Y.; Wierzbicki, T. A comparative study of three groups of ductile fracture loci in the 3D space. *Eng. Fract. Mech.* **2015**, *135*, 147–167. [CrossRef]
15. Fincato, R.; Tsutsumi, S. Numerical modeling of the evolution of ductile damage under proportional and non-proportional loading. *Int. J. Solids Struct.* **2019**, *160*, 247–264. [CrossRef]
16. Murakami, S. *Continuum Damage Mechanics*; Springer: Berlin/Heidelberg, Germany, 2012; pp. 111–138.
17. Hering, O.; Dahnke, C.; Tekkaya, A.E. Influence of Damage on the Properties of Cold Forged Parts. In Proceedings of the 51st ICFG Plenary Meeting (ICFG 2018), Ohio, OH, USA, 21–24 October 2018; pp. 137–144.